JOURNAL OF THE AMERICAN CHEMICAL SOCIETY

Article

Universal Oxide Shell Growth Enables In-situ Structural Studies of Perovskite Nanocrystals during the Anion Exchange Reaction

Anna Loiudice, Michal Strach, Seryio Saris, Dmitry Chernyshov, and Raffaella Buonsanti

J. Am. Chem. Soc., **Just Accepted Manuscript** • DOI: 10.1021/jacs.9b02061 • Publication Date (Web): 02 May 2019

Just Accepted

ACS Publications

is published by the American Chemical Society. 1155 Sixteenth Street N.W., Washington, DC 20036

Universal Oxide Shell Growth Enables In-situ Structural Studies of Perovskite Nanocrystals during the Anion Exchange Reaction

Anna Loiudice,[†] Michal Strach,[†] Seryio Saris,[†] Dmitry Chernyshov,[⊥] Raffaella Buonsanti[*†]

[†] Laboratory of Nanochemistry for Energy Research, Institute of Chemical Sciences and Engineering, Ecole Politechnique Fédérale de Lausanne, Sion, CH-1950, Switzerland.

[⊥] The Swiss-Norvegian Beamline (SNBL) - ESRF CS40220, 38043 Grenoble CEDEX 9, France.

*Correspondence to: raffaella.buonsanti@epfl.ch

ABSTRACT

The ability to tune core@shell nanoparticles is desirable for many applications, yet it remains a key synthetic challenge especially when the shell is a metal oxide. In this work, we introduce a general colloidal atomic layer deposition (c-ALD) synthesis to grow an alumina shell with tunable thickness around a nanocrystalline core of various compositions spanning from ionic semiconductors (i.e., $CsPbX_3$, with X=Br, I, Cl) to metal oxides and metals (i.e., CeO_2 and Ag). The distinctive properties of each core (i.e., emission, surface chemistry, stability) allowed to optimize and to elucidate the chemistry of the c-ALD process. Compared to gas phase ALD, this newly developed synthesis has the advantage of preserving the colloidal stability of the nanocystalline core while controlling the shell thickness from 1 nm to 6 nm. As one example of the opportunities offered by the growth of a thin oxide shell, we study the anion exchange reaction in the $CsPbX_3$ perovskites nanocrystals by in-situ X-ray diffraction, a study impeded so far by the instability of these class of materials and by the fast exchange kinetics.

INTRODUCTION

Metal oxide core@shell nanoparticles are pivotal for many areas of science, including medicine, biology, optics, electronics, energy storage and catalysis.[1-4] Most oxide shells are prepared via hydrolysis/condensation reactions, with one representative example being the so-called Stober method where tetraethylortosilicate is used as the precursor for the growth of silica shells.[5,6] The main drawbacks of the available wet-chemistry approaches are the encapsulation of multiple nanoparticles within the same shell, which results in micron-size powders as the final product, and the poor control over the shell thickness below 5 nm.[7-9] Yet, thinner oxide layers are interesting when the aim is to manipulate the communication of the core with the external environment rather than to completely isolate it (i.e., charge transfer or diffusion of atomic species across the shell). One must turn to atomic layer deposition (ALD) in gas phase to achieve control and tunability at the atomic scale over conformal oxide layers.[10-12] However, gas-phase ALD suffers from some limitations such as the difficult control over the amount of precursor, which is dictated by the pressure range covered in the reactor, and the loss of colloidal stability in the case of powder reactors. Colloidal ALD (c-ALD) allows to overcome these issues, however its potential has been mostly limited to the synthesis of chalcogenide core@shell nanoparticles.[13-17] Pioneering work in the field has been carried out by Itthuria and co-workers with other follow-ups reported in the literature.[14-17] In these studies, the ALD process starts with the functionalization of the nanocrystalline core surface with inorganic ligands (e.g. S^{2-}, Se^{2-}, $Sn_2S_6^{4-}$, etc.) followed by the addition of the chalcogenide precursor.[14-17]

Here, we propose a general c-ALD synthesis to grow a metal oxide shell, exemplified by aluminum oxide (AlO_x), around a nanocrystalline core of different composition, including semiconductors (i.e. $CsPbX_3$, with X=Br, I, Cl), metals (i.e. Ag) and metal oxides (i.e. CeO_2).

AlO_x was chosen because it is among the most studied metal oxides obtained by gas phase ALD and for direct comparison with our previous work on gas phase ALD for $CsPbX_3$.[10-12] During the c-ALD, trimethylaluminum (TMA) and pure oxygen are sequentially injected at room temperature in the octane solution containing the nanocrystals (NCs). Infrared spectroscopy reveals that the nucleation of AlO_x on the NC surface occurs on an oxygen site. By combining different techniques, including electron microscopy and dynamic light scattering, we observe a layer-by-layer growth of the alumina shell which is tailored from 1 nm up to 6 nm.

Then, we demonstrate the advantage of the as-synthesized alumina shell to study nanoscale chemical transformations by focusing on the anion exchange reaction in $CsPbX_3$ NCs. To date, remarkable studies on ion-exchange in NCs have been performed, mostly focusing on cation exchange (i.e., CdSe to Ag_2Se, CdS to PbS NCs, PbS to PbS core-shell CdS and $Cu_{2-x}S$ to $CuInS_2$).[18-22] Only recently, with the booming of perovskites in solar cells and lighting applications, anion exchange reactions have attracted increasing interest in the chemistry community.[23-30] The facile and fast anion exchange occurring in both NCs and bulk perovskites (i.e. $CsPbBr_3$ to $CsPb(Br_yCl_{1-y})_3$ or $CsPb(Br_yI_{1-y})_3$) plays an important role in photostability, anomalous hysteresis and light induced segregation.[31-35] Despite the tremendous interest in understanding such phenomena, the ion diffusion mechanism in perovskite is still largely unknown. Because of the fast anion exchange kinetics (completed at the time scale of seconds), the few studies conducted so far have used optical probes, which provide only indirect proofs of structural changes.[36-38] In this article, thanks to the AlO_x shell around the $CsPbX_3$ NCs, the anion exchange reaction is slowed down by an order of magnitude and in-situ X-ray diffraction (XRD) studies could be performed. The temporal evolution of the NC structure during the reaction reveals anomalous alloy properties of the

halide perovskites compared to conventional semiconductors, in agreement with a recent theoretical study.[39]

EXPERIMENTAL SECTION

Chemicals. All chemicals were purchased from Sigma Aldrich and used without purification, unless specified. Cesium carbonate (Cs_2CO_3, 99.9%), lead (II) bromide ($PbBr_2$, 99,99%, Alfa Aesar), lead (II) iodide (PbI_2 99.9985%, Alfa Aesar), lead (II) chloride ($PbCl_2$, 99.99%), oleic acid (OLAC, technical grade 90%), oleylamine (OLAM, technical grade 70%), 1-octadecene (ODE, technical grade 90%), octane (anhydrous, ≥99%), toluene (anhydrous, ≥99%), N,N-dimethylformamide, (DMF, anhydrous, ≥99%), methyl acetate (MeOAc, anhydrous 99.5%), Cerium (III) nitrate hexahydrate ($Ce(NO_3)_3$•$6H_2O$ (99%)), Silver nitrate ($AgNO_3$), trimethyloxoniumtetrafluoroborate (Me_3OBF_4) and Trimethylaluminium (98%, Strem).

Material Synthesis. *Synthesis of Cs-oleate (Cs-OLA) precursor:* 0.8 g of Cs_2CO_3, 2.5 mL OLAC and 80 mL ODE were added to a 100 mL 3-necked round bottom flask and stirred under vacuum for 1h at 120 °C. The flask was purged with N_2 for 10 min and then placed back under vacuum. This process of alternately applying vacuum and N_2 was repeated for a total of 3 times to remove moisture and O_2. The reaction temperature was increased to 150ºC and kept at this temperature until the solution was clear, indicating that the Cs_2CO_3 has completely reacted with the OLAC. The Cs-OLA solution in ODE was stored in N_2 until needed for the NC synthesis. This Cs-OLA was used for the synthesis of $CsPbBr_3$ and $CsPbCl_3$ NCs. Instead for the synthesis of $CsPbI_3$ NCs the amount of reagents was slightly different: 0.25 g of Cs_2CO_3, 1 mL OLAC and 25 mL ODE, while the procedure was kept the same.

$CsPbX_3$ NCs synthesis. $CsPbX_3$ NCs were synthesized with slight modification from the one previously reported by Protesescu et al.[40] For the synthesis of $CsPbBr_3$ and $CsPbCl_3$ NCs:

$PbBr_2$ (0.21 g) or $PbCl_2$ (0.26 g) and ODE (15 mL) were stirred in a 50 mL round bottom flask and degassed under vacuum at 120 °C for 1 h. The flask was then filled with N_2 and kept under constant N_2 flow. OLAC and OLAM (1.5 mL each) were injected and the mixture was kept at this temperature until all the $PbBr_2$ was dissolved. The temperature was then increased to 165 °C. The Cs-OLA (1.2 mL) precursor, pre-heated to 100 °C under N_2 atmosphere, was swiftly injected into the reaction mixture. The reaction mixture turned yellow or white and the reaction was quenched by immediate immersion of the flask into an ice bath (~5 s after injection). The synthesized NCs were precipitated by centrifugation at 6000 rpm for 30 min, the supernatant was removed and the NCs were re-dissolved in 1.5 ml of hexane. A second wash was carried out by adding ethyl acetate in a ratio 1:1 with hexane, the mixture was centrifuged and the precipitate was dissolved in octane obtaining a final concentration of ~10 mg/ml. The synthesis of $CsPbI_3$ NCS was carried in the same way with some modification in the amount of reagent used: PbI_2 (0.70 g), 35ml ODE, OLAC and OLAM 3.5 each and 5.6ml of Cs-OLA prepared as described previously was injected. Methyl acetate was used for the second washing as reported by A. Swarnkar et al..[41]

CeO_2 NCs synthesis. CeO_2 NCs were synthesized by following a previously reported procedure.[42] 1 mmol of $Ce(NO_3)_3 \cdot 6H_2O$ was mixed with 1 mL of OLAM in 6.3 mL of ODE at room temperature and dissolved at 80ºC for 30 min. CeO_2 NCs were grown by heating the mixture at 260ºC for 2h. The as-prepared NCs were purified by washing, precipitation and centrifugation cycles, using ethanol, acetone and hexane at least 4 cycles to remove any unreacted cerium precursor, surfactants, and excess ODE. The resultant dark brown precipitate was re-dispersed in octane in a concentration of around 10 mg/ml.

Ag NCs synthesis. Ag NCs were synthesized by following a previously reported procedure.[43] 1 mmol $AgNO_3$ was mixed with 20 ml OLAM at room temperature followed by heating up to 60°C, which was maintained until the granular $AgNO_3$ crystals were completely

dissolved. The solution was then quickly heated up (≥10°C/min) to 180°C and the temperature was maintained for 1hr before the reaction system was cooled down to room temperature. The resulting dark-brown solution was washed with acetone and re-dispersed in octane. Size-selective precipitation was used to narrow their size distribution.

Ligand Exchange on Ag NCs. Ag NCs with OLAC as ligand were obtained by using a reported ligand-stripping procedure.[44] 1ml of acetonitrile containing MeO_3BF_4 was added to 1ml of Ag NCs with native OLAM ligands (Ag-OLAM NCs) dispersed in hexane (with a concentration of 10 mg/ml by ICP-OES); after 1 min stirring, 1 ml of toluene was added and the mixture was centrifuged to allow NCs precipitation. The obtained NCs were dispersed in 1 ml DMF. Successively 1ml of hexane containing OLAC was added to the NCs dispersed in DMF and after 1 min stirring, the NCs were precipitated and re-dispersed in octane. Ag NCs with oxidized surface (Ag-AgO_x NCs) were obtained by flowing for 1hr pure O_2 gas into the Ag-OLAM NC solution.

c-ALD synthesis. In a 3-necked flask a solution of NCs (typically 150 μl of NCs solution with a concentration of 5 mM) dissolved in octane as the solvent was gently stirred under N_2 flow. An extra amount of octane (typically 2 ml) was added so to ensure good NCs separation and to guarantee an homogeneous shell growth. **Figure S1** in the supporting information (SI) sketches the synthesis set-up. One c-ALD cycle consists of: 1) drop-wise addition of TMA diluted in octane to the NC solution (the optimized rate of the syringe pump was fixed at 1ml/h); 2) 5 min waiting time so to ensure that the reaction in step 1) was completed; 3) addition of O_2 gas by mean of a mass flow controller; 4) 5 min waiting time. This cycle is repeated n-times to reach the desired thickness. The optimal amount of TMA (80 μl from a diluted TMA solution in octane with a concentration of $0.4*10^{-3}$ μM) to add each cycle was obtained by monitoring the change of the $CsPbX_3$ NCs' optical properties upon addition of increasing amount of TMA (**Figure S2**). The optimal amount could slightly change from

batch to batch. The full process was automated by a home-made Lab-View software where precursor amount, injection speed, and waiting time are independently defined. Different c-ALD conditions were tested to optimize the process (**Figure S3**). In order to retain the colloidal stability in the organic solvent of the as-synthesized core@shell NCs, OLAC was introduced in place of TMA after 8-10 cycles. This step functionalizes the surface of the shell which can continue to grow without any precipitation of the NCs. A gas tight syringe was used for the TMA injection to ensure that the TMA concentration stayed unchanged during the full process. The TMA is used in very diluted amount to avoid any safety issue.

Characterizations. *Electron Microscopy.* Transmission electron microscopy (TEM) images were acquired on a FEI Tecnai-Spirit at 120 kV. High-angle annular dark-field scanning TEM (HAADF-STEM) images and X-ray energy dispersive (EDX) elemental maps were acquired on a FEI Tecnai-Osiris at 200 kV. This microscope is equipped with a high brightness X-FEG gun, silicon drift Super-X EDX detectors and a Bruker Esprit acquisition software. Samples were prepared by dropping hexane or octane solution containing the nanoparticles on the surface of ultrathin carbon-coated copper grids (Ted Pella, Inc.).

Optical Spectroscopy. All optical measurements including photoluminescence (PL) emission spectra, time-resolved fluorescence lifetimes (TRPL) and quantum yield (QY) measurements were collected on a Horiba Jobin Yvon Fluorolog-3 with a PMT as detector. The crude $CsPbX_3$ NC solutions were diluted in octane to reach an optical density of about 0.1-0.2 at the excitation wavelength. For the TRPL the excitation source is a Horiba nanoLED-370 with an excitation wavelength of 369 nm, a pulse duration of 1.3 ns and a repetition rate of 100 kHz. The absolute QY measurements were performed in the integrating sphere Fluorolog-3 accessory where a quartz cuvette containing the sample was placed. The sample was excited with a monochromated xenon lamp at 470 nm. The emitted light was collected at the exit of the sphere by a PMT detector. For each sample, four measurements

were performed: (i) the sample emission (S_{em}) that collect the photons emitted by the sample; (ii) the blank emission (B_{em}) that collects the emission from the cuvette containing only the solvent; (iii) the sample excitation (S_{exc}), that records the photons at the pumping wavelength that are not absorbed by the sample; (iv) the blank excitation (B_{exc}), that records the photons at the pumping wavelength through the blank. The QY was then calculated as:

$$QY(\%) = \frac{S_{em} - B_{em}}{B_{exc} - S_{exc}} \times 100$$

Any reabsorption correction factor was neglected in our calculation of QY, since the solutions investigated were diluted to the point that reabsorption of the PL could be neglected. The final reported QY are an average over 3 measurements.

UV−vis absorption measurements were performed in transmission mode using a PerkinElmer Lambda 950 spectrophotometer equipped with a deuterium lamp as a light source for the ultraviolet range and a tungsten halide lamp as a light source for the visible and infrared range, and a PMT with a Peltier-controlled PbS detector.

Dynamic Light Scattering (DLS). DLS measurements were carried out using a Zetasizer Nano ZS (Malvern) instrument. The Nano ZS system is equipped with a 4 mW red laser (633 nm) and a detection angle of 173°. The samples were prepared in a quartz cuvette in octane solvent. For each sample 3 measurements were performed with a fixed run time of 10s. The Malvern DTS 5.10 software was applied to process and analyze the data.

Attenuated Total Reflectance-Fourier Transform Infrared Spectroscopy (ATR-FTIR). ATR-FTIR was performed using a Perkin Elmer instrument Spectrum 100 by drop-casting 30 μl of the NC solution on the ATR window, and measured with a resolution of 4 cm^{-1}.

Inductively Coupled Plasma - Optical Emission Spectrometry (ICP-OES). ICP-OES was performed on Agilent 5100 model to determine the $CsPbX_3$ NCs, CeO_2 NCs and Ag NPs concentration. 5 standard solutions of Pb, Ce and Ag were prepared to obtain the calibration curve used to determine the concentrations of the digested nanocrystal solution. The sample

solution was prepared by dissolving the nanocrystals in 70% HNO_3 followed with the addition of a specific amount of ultrapure water until the solution reaches the 2% acid content needed for the analysis.

Synchrotron set-up. The series of in-situ XRD experiments were carried out at Swiss-Norwegian beamline BM01 at ESRF in Grenoble (France). We used a custom-made capillary flow cell and two syringe pumps to inject the different NCs into the probed volume within a glass capillary (**Figure S4**). The XRD patterns were recorded with a PILATUS 2M detector. We started acquiring XRD data 10 s before the injection took place, one pattern each 2.5 seconds. Details of the beamline and equipment have been described elsewhere.[45] A lambda of 0.64066 Å was used for all the experiments. The spot size was adjusted to the capillary size (1.5 mm external diameter, 0.01 mm wall thickness). The diffraction patterns were analyzed using TOPAS 5.[46] The calibration of diffractometer parameters was done with LaB_6 NIST standard and PyFai software.[47] The raw data were processed into powder patterns with Bubble.[45] To monitor the evolution of the lattice parameters, all patterns were fitted using the Le Bail method. The utilized crystallographic data were taken from the ICSD database: $CsPbBr_3$ (Pm-3m, collection code: 97852), $CsPbI_3$ (Pm-3m, collection code: 161481), and $CsPbCl_3$ (Pm-3m, collection code: 29067).

RESULTS AND DISCUSSION

In a typical experiment, the optimal amount of TMA diluted in octane is added drop-wise to a NC solution; after a reaction time of 5 minute, O_2 gas is introduced followed by other 5 min waiting time (see Experimental Section for details). These steps constitute one cycle, which is then repeated multiple times. We observed that after a certain number of cycles (typically 8-10 cycles) the as-synthesized core@shell NCs would lose their colloidal stability. In order to prevent this issue, when this stage is reached, OLAC is added in place of the O_2 to

prevent the formation of any precipitate. The whole c-ALD synthesis is illustrated in **Figure 1**. The proposed procedure mimics the gas-phase ALD process by translating it into solution. Similarly, to the gas-phase ALD, the repetition of sequential steps multiple times is adopted to precisely control the thickness of the metal oxide shell resulting in a core@shell NC structure. The generality of the proposed approach is demonstrated by growing the AlO_x shell on various NC cores in terms of composition and intrinsic properties. As we discuss later, these NC cores have distinctive characteristics that combined all together helped to elucidate different aspects of the developed c-ALD synthesis.

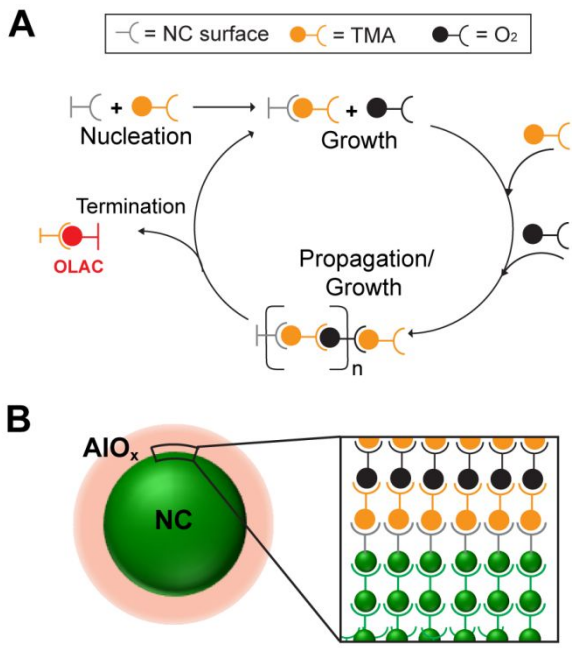

Figure 1. A) Schematic of the c-ALD synthesis and B) sketch of the obtained core@shell NCs.

Figure 2 gives an overview on the synthesized core@shell NCs with different compositions (i.e., $CsPbBr_3$@AlO_x, CeO_2@AlO_x, Ag@AlO_x NCs) characterized by electron microscopy and DLS. The HAADF-STEM images with the corresponding EDX maps in **Figure 2A-E** and the low magnification TEM images in **Figure S5** evidence the preservation of the size and shape of the inorganic core which is surrounded by a lower density alumina

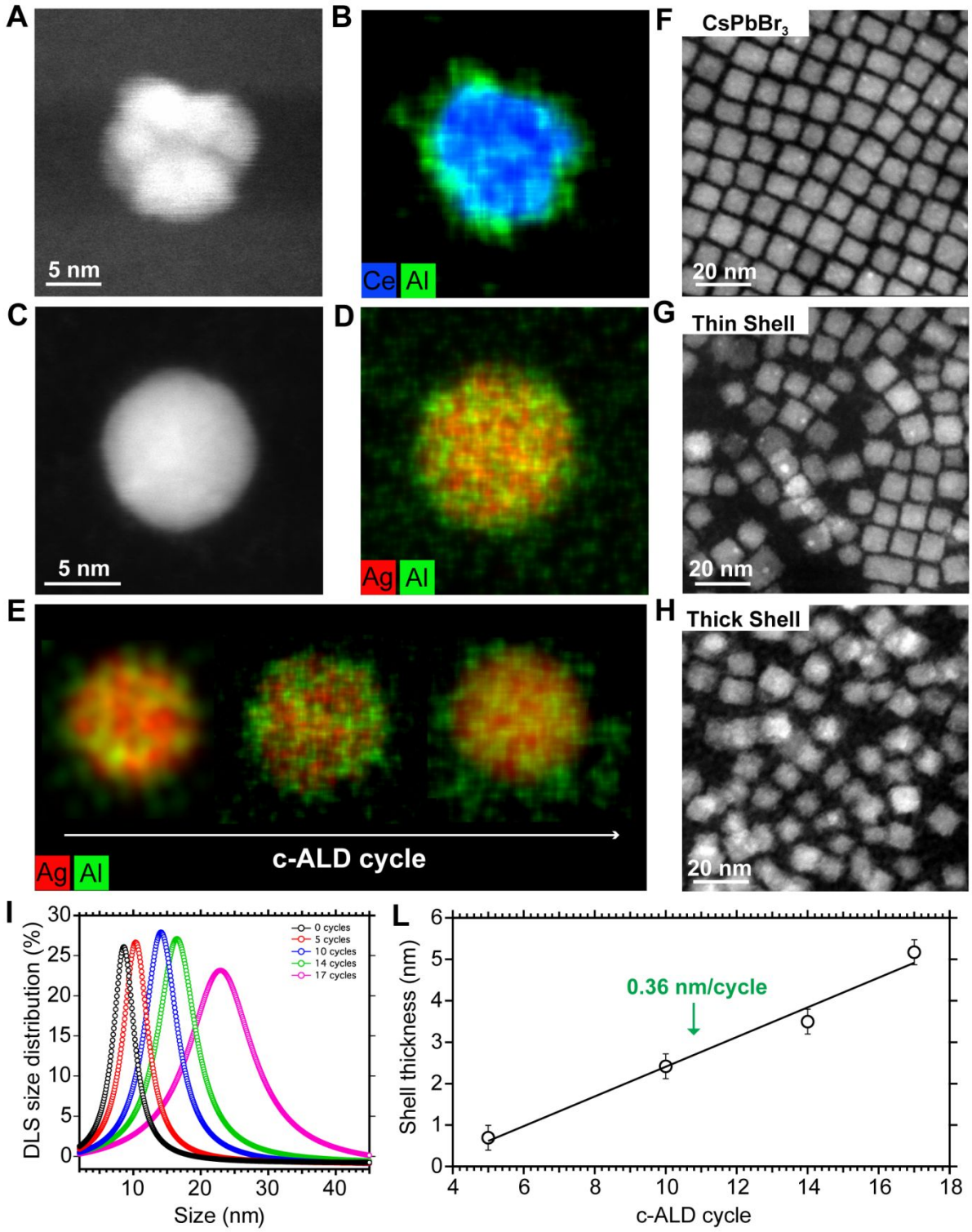

Figure 2. HAADF-STEM images and corresponding EDX coloured maps of A,B) CeO_2@AlO_x and C,D) Ag@AlO_x NCs; E) EDX maps of Ag@AlO_x NCs obtained at different c-ALD cycles. F,G,H) HAAFD-STEM images of $CsPbBr_3$@AlOx NCs without any shell, with thin (8 cycles) and thick (17 cycles) AlO_x shell respectively; I) DLS size distribution of $CsPbBr_3$@AlO_x NCs obtained by performing 0, 5, 10, 14, and 17 c-ALD cycles; L) The calculated shell thickness estimated by DLS measurements as a function of c-ALD cycles fitted with a linear curve (black line). From the slope of the fitted curve a growth rate of 0.36 nm/cycle is estimated.

shell whose thickness increases with the number of cycles (**Figure 2E**). The presence of the AlO_x shell around each single NC core is further evidenced by the strong contrast between the cubic assemblies of the as-synthesized $CsPbBr_3$ NCs on the TEM grid and the highly disordered one for the $CsPbBr_3$@AlO_x core@shell NCs (**Figure 2F-H**). For the $CsPbBr_3$ NCs, characterization EDX mapping cannot provide clear information regarding the presence of the Al in the shell because of the overlap between Br and Al peak in the spectrum (**Figure S6**). Thanks to the preservation of colloidal stability of the core@shell NCs, DLS was used to estimate the AlO_x shell thickness vs. the number of cycles (**Figure 2I,L**) and allowed to determine the overall growth rate on the NCs. The results show a fine-tuning of the shell thickness ranging from 1 nm to 6 nm and an estimated growth rate during the c-ALD of around 0.36 nm/cycle. The average bond length Al-O-CH_3 is around 0.30±0.11 nm (min = 0.29 nm and max = 0.38 nm based on a CSD search comprising 2892 structures) thus approximately corresponds to the growth rate we have measured in our system. The similarity between the measured AlO_x growth rate and the estimated bond length suggests that each cycle correspond to the growth of a single layer around the NC core.

The optical properties of the $CsPbBr_3$ NC cores were studied to assess the preservation of their structure and composition (**Figure S7**). The AlO_x was found to even improve the stability and the photoluminescence quantum yield (QY) of the final $CsPbBr_3$@AlO_x NCs which is three times higher compared to the uncoated counterpart, suggesting that surface shallow trap passivation occurs during the first c-ALD cycle, also evident by the increased lifetime (**Figures S8, S9** and **Tables S1,S2**). The changes of QY with the amount of TMA added in the solution were used to calibrate the optimal amount of TMA to be added in each c-ALD cycle (**Figure S2, S3** for details regarding the optimization process by tuning injection time, waiting time, temperature). FTIR analysis was performed on the core@shell NCs to characterize the AlO_x structure (**Figure S10**). C-H vibrational peaks corresponding to

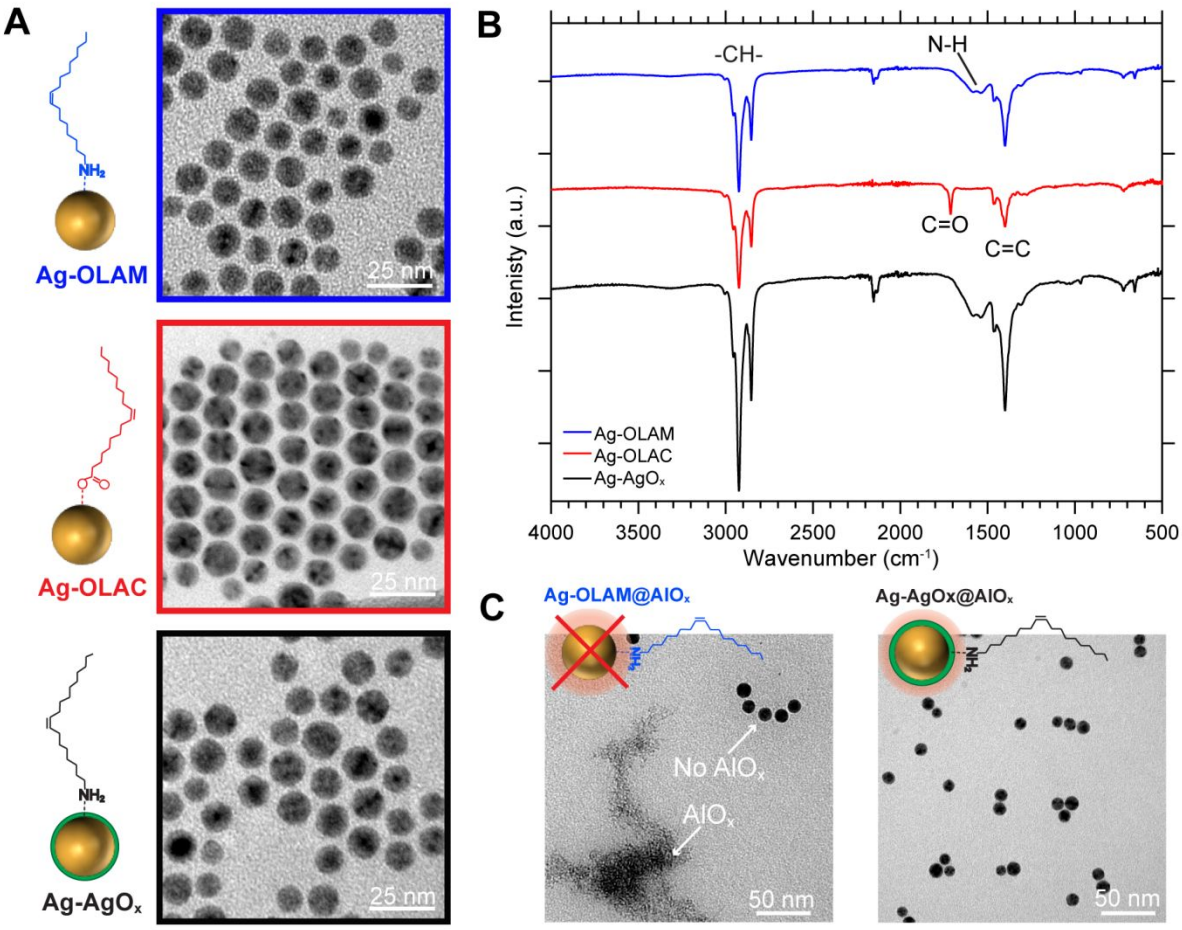

Figure 3. A) TEM images of the Ag NCs with different surface chemistry along with a representative sketch: Ag-OLAM (blue), Ag-OLAC (red) and Ag-AgO (black); B) FTIR spectra of the samples in A); C) TEM images of the obtained Ag-OLAM@AlO_x (left) and Ag-AgO_x@AlO_x (right) NCs.

the NC native ligands are still present after the c-ALD, suggesting that the ligands are not removed during the c-ALD process but are rather trapped in the AlO_x shell. Instead, the new features at lower wavenumbers were associated with the presence of an amorphous AlO_x shell.

The FTIR shows that the organic ligands are still present after the c-ALD. At the same time, oxygen sites (or more rarely other chemical groups) are required to initiate the ALD by reacting with the TMA. To elucidate the role played by the ligands functionalizing the NC core during the nucleation and growth of the AlO_x shell, the Ag@AlO_x NCs were chosen as the model system because of their robustness and versatile surface chemistry compared to the

$CsPbX_3$ and the CeO_2 NCs. Moreover, the metallic nature of the Ag NCs allows to study the role of surface oxidation considering that Ag is relatively easy to oxidize.[48,49] Starting from the as-synthesized Ag NCs that have OLAM as ligands (Ag-OLAM NCs), Ag NCs functionalized with OLAC (Ag-OLAC NCs) were obtained by performing a mild ligand exchange. Instead, Ag NCs with an oxidized surface (Ag-AgO_x NCs) were obtained by flowing pure O_2 gas in the Ag-OLAM NC solution.[48,49] The UV-Vis absorption spectra (**Figure S11)** evidenced a slight red shift in the plasmon peak consistent with the formation of a thin oxide shell around the Ag-OLAM NCs. **Figure 3A,B** shows the corresponding TEM images and FTIR spectra of the Ag NCs with the three different surface chemistry. The peaks at 1714 cm^{-1}, which is characteristic of the C=O stretching, and 1405 cm^{-1}, which corresponds to the C=C stretching, evidence the monodentate binding of OLAC on the Ag NC surface. Ag-OLAM NCs and Ag-AgO_x NCs possess the IR signature typical of OLAM functionalization. An equal number of c-ALD cycles (8 cycles) was performed on these Ag NCs. **Figure 3C** shows that when c-ALD is performed on Ag-OLAM NCs the AlO_x nucleates in solution heterogeneously, thus separated from the Ag NCs. On the contrary, the AlO_x shell grows on both Ag-OLAC and Ag-AgO NCs surface. These results demonstrate that oxygen, whether on the surface of the NCs or in a monodentate ligand like OLAC, initiates the c-ALD by reacting with the TMA during the first cycle (**Figure S12**). Furthermore, **Figure S10** shows that the C=O stretch almost disappears in the Ag-OLAC@AlO_x NCs, which points to the breaking of the double bond following the reaction with the TMA.

Having demonstrated that we can successfully grow a tunable metal oxide shell on NCs with different composition as long as oxygen atoms are present on their surface, it is interesting to explore the new opportunities open by this general synthesis to study the communication of the inner core with its surroundings. Solid-state transformations via

diffusion at the nanoscale are difficult to investigate especially when the kinetics are too fast to allow structural characterization. The anion exchange reaction in $CsPbX_3$ NCs is of particular interest for the present work. As aforementioned, the understanding of this phenomena is very relevant to device implementation and performance, in addition to fundamental science.[31-35] Yet, because of the ion exchange occurring within seconds, only optical probes have been used so far.

To closely monitor the structural change occurring during the anion-exchange, $CsPbX_3$ NCs should mix rapidly and reproducibly to ensure a homogeneous environment during the reaction while allowing the X-rays to capture structural information. These requirements were fulfilled by building a home-made set-up where two NC solutions of different composition react in a capillary (see Experimental Section and **Figure S4** for details). In our experiments, the solution of the $CsPbX_3$@AlO_x NCs with different shell thicknesses and composition, all in anhydrous octane, were simultaneously injected through a mixing frit placed at the entrance of the reaction chamber (i.e., the capillary) in which the two $CsPbX_3$ NCs have a few sub-milliseconds to mix. This time is shorter than the time needed for the exchange to come to completion, which varies from seconds to tens of minutes depending on the investigated NCs (composition and w/o shell) as discussed later. After the injection, the structural changes occurring during the exchange were monitored in real time by acquiring XRD patterns every 2.5 s. The combination of sub-millisecond mixing time, the millisecond acquisition time permitted by synchrotron radiation, the fact that the AlO_x shell slows down the reaction kinetics and the high resolution data with a high signal-to-noise ratio, enabled us to follow the structural evolution of the $CsPbX_3$ NCs during the anion exchange reaction. To the best of our knowledge this is the first time that such kind of studies are reported.

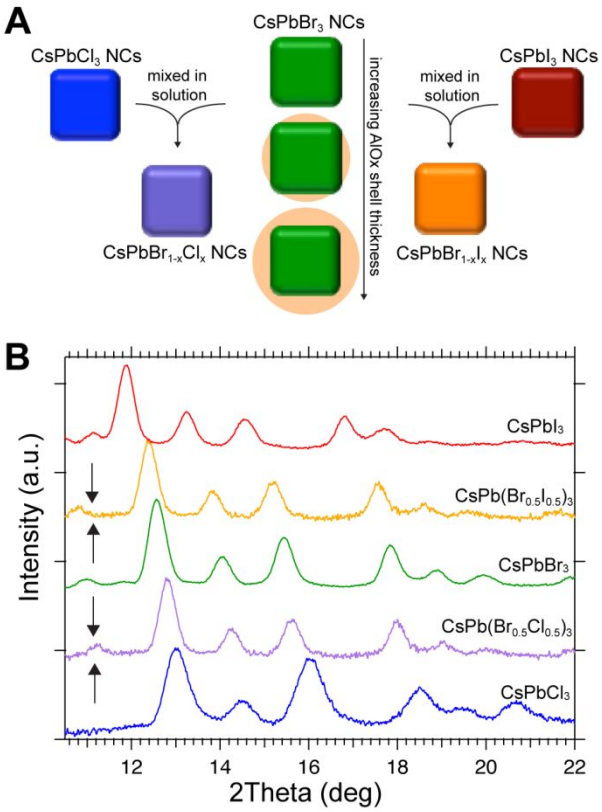

Figure 4. A) Schematics of the anion exchange reactions investigated during the in-situ X-ray diffraction experiments; B) XRD spectra of the as-synthesized $CsPbX_3$ NCs used in the synchrotron experiments together with the XRD spectra of the final products: $CsPb(Br_{0.5}I_{0.5})_3$ and $CsPb(Br_{0.5}Cl_{0.5})_3$ NCs.

Figure 4A summarizes schematically the in-situ experiments that were performed. Specifically, $CsPbBr_3$@AlO_x NCs with two different AlO_x shell thickness (**Figure 2F-H**) constitute one of the reagents and they will be referred to as Br/no-shell, Br/shell**1** and Br/shell**2**, respectively. As the second reagent, $CsPbCl_3$ NCs, $CsPbI_3$ NCs and $CsPbI_3$@AlO_x shell1 NCs (named Cl/no-shell, I/no-shell and I/shell**1**) were selected. The XRD patterns of the uncoated $CsPbX_3$ NCs used in this work together with the XRD pattern obtained for the final exchanged product ($CsPb(X_{1-y}Br_y)_3$ NCs with X=I or Cl) are reported in **Figure 4B**, which evidence that the different composition $CsPbX_3$ NCs are characterized by distinguished diffraction features. The corresponding core@shell NCs have similar XRD patterns (data not shown). The initial concentrations of the NCs in the mixture were adjusted so that the final product will result in a mixed halide with 1:1 ratio. **Figure S13** shows that all

the NCs used during the in-situ experiment have an average edge size of 7.5 nm, so to exclude that any broadening of the XRD peaks is due to inhomogeneity in the NC size.

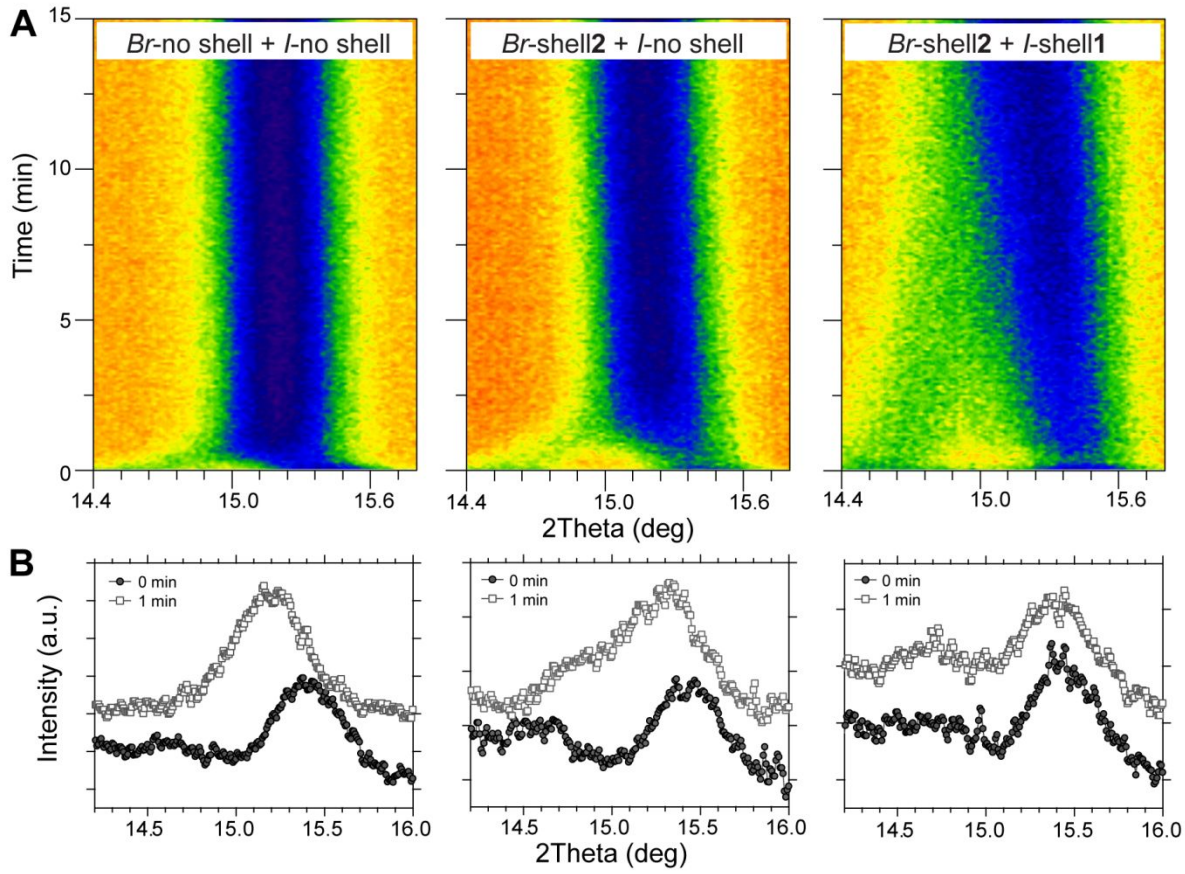

Figure 5. A) Representative 2D maps from the in-situ XRD experiments illustrating the changes observed in the selected 2Theta range during the reaction from $CsPbBr_3@AlO_x$ to $CsPb(Br_{0.5}I_{0.5})_3$ with increasing AlO_x shell thickness, specifically: Br-no shell/ (left), Br-shell**2**/Br-no shell (centre), and $CsPbBr_3@AlO_x$ shell**2**/$CsPbI_3@AlO_x$ shell1 (right); B) Snapshots at time=0 min and time=1 min from the maps in A).

A representative data set of the temporal evolution of the XRD patterns during the reaction from $CsPbBr_3@AlO_x$ NCs to $CsPb(Br_{0.5}I_{0.5})_3$ NCs with various AlO_x shell thicknesses is shown in **Figure 5A**. The maps report the time evolution of the two reagents in a selected region of the XRD spectrum between 14.5 and 15.7 degrees which allows one to monitor the (211) diffraction peak from [$CsPbBr_3@AlO_x$ NCs + $CsPbI_3@AlO_x$ NCs] at time 0 to the final $CsPb(Br_{0.5}I_{0.5})_3$ composition. For clarity, the corresponding XRD patterns acquired at time 0 and 1 min for these three mixtures are shown in **Figure 5B**. It is immediately evident that the

thicker the AlO_x shell, the slower the anion exchange reaction, because no change in the XRD pattern is observed after 1 minute for the thicker shell.

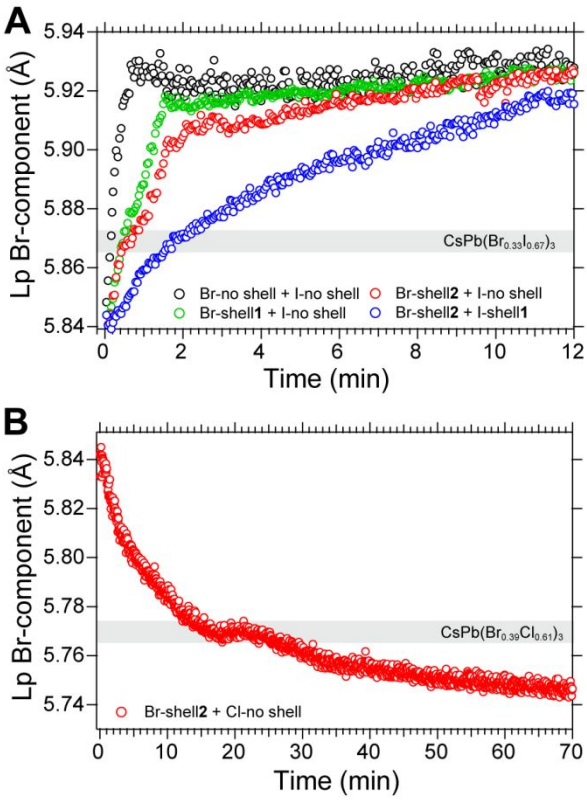

Figure 6. A) Time evolution of the lattice parameters for the $CsPbBr_3$ NCs (Lp Br-component) with increasing shell thickness when reacting with $CsPbI_3$ NCs, specifically: Br-no shell/ I-no shell (black), Br-shell**1**/I-no shell (green), Br-shell**2**/I-no shell (red), and Br-shell**2**/I-shell**1** (blue); B) Time-dependent change of the Lp for the Br-shell**2** in presence of uncoated $CsPbCl_3$ NCs.

The good separation between the XRD peaks allows for Le Bail refinement. The temporal evolution of the lattice parameters (Lp) obtained from the refinement for all the different mixtures are reported in **Figures 6A,B** and **S14**. In particular, for the mixture Br/shell**2** and I/shell**1** the final product composition is obtained after more than 12 min compared to only 1 min in the case of uncoated $CsPbBr_3$ and $CsPbI_3$ NC mixtures (**Figure 6A**). Similar experiments were conducted for the mixture with $CsPbCl_3$ NCs (**Figure 6B, S14**). In the latter case, the anion exchange reaction between Cl^- and I^- is much slower in agreement with

the data obtained by optical probing.[36-38] In particular, for the mixture Br/shell**2** and Cl/no shell in **Figure 6B**, the reaction reaches completion after 70 min.

Focusing on the change of Lp over time for the two cases of Br to BrI and of Br to BrCl, some key information were extracted. First of all, the experiments conducted on the uncoated $CsPbX_3$ NC mixtures evidence a very fast structural evolution resulting in an exponential increase of the Lp with time for Br to BrI and in an exponential decrease of the Lp for Br to BrCl (black curves in **Figure 6A** and **Figure S14**). Second, the temporal evolution of the Lp in the mixture containing $CsPbX_3$@AlO_x NCs reveal a more complex behaviour for both iodine and chlorine exchange (**Figure 6A,B**). In particular, after an initial steady change of the Lp, a deviation from the exponential trend is noticed and a bump, corresponding to the Lp remaining constant for a certain time, is observed. For the iodine exchange, the Lp stays constant at a value of 5.867 Å for a short time (around 10 seconds), to then start to change again with a slower rate of exchange (**Figure 6A**). While the AlO_x shell thickness determines the time at which the deviation from the exponential trend occurs (i.e. thicker shell, longer time), the bump is observed always at the same Lp value (highlighted as a grey area in **Figure 6A**). A similar behaviour is observed also for the chlorine exchange wherein after around 20 minutes the lattice parameter stabilizes at a value of 5.768 Å and then starts to change with a slower rate of exchange (**Figure 6B**). Noteworthy, the change in the rate of exchange occurs in both cases at a specific $CsPb(Br_yI_{1-y})_3$ and $CsPb(Br_yCl_{1-y})_3$ composition, where y = 0.33 and 0.39 for iodine and chlorine exchange respectively. These results suggest that the two systems undergo a similar anion exchange mechanism, where at a certain mixed halide ratio a more stable structure is formed and this structure is kept until new ions are incorporated into the structure, and the Lp starts to change with a slower rate until the final composition is obtained. These results can be explained by referring to a recent theoretical study by W.-J. Yin et al..[39] The authors used first-principle calculations together with cluster-

expansion methods to study the structural properties of mixed halide perovskites. They find that halide perovskites exhibit anomalous alloy properties compared to conventional semiconductors; specifically, they find that a particular stable alloy structure exist for specific composition with formation energies lower than other structures. They calculated a minimum of formation energy for y=1/3 that is very close to the composition (y= 0.33 and 0.39 for iodine and chlorine exchange) where we observe that the lattice parameters have the anomalous change in the rate of ion exchange. The reason for this is that halide perovskite have a strong ionic characters, so Coulomb interactions plays a major role in this case, which lowers the formation energy and favours certain structures. It is interesting to compare our results from the in-situ structural analysis with those obtained from the in-situ optical monitoring of the anion exchange reaction reported by Kosher et al.[36] Here, the authors study the exchange kinetics for uncoated $CsPbBr_3$ NCs mixed with I-oleate and Cl-oleate solutions by following the band gap change. They observe a very similar trend for the Br-to-Cl transformation, with distinct intervals of constant bandgap which closely resembles our structural data and which are attributed to a transient structure. Instead, for the Br-to-I exchange, the faster exchange kinetics prevents to catch this intermediate transformation and the authors conclude that two different exchange mechanisms are taking place in the two systems. These contrasting results compared to our data reinforce the need to slow down the reaction in order to correctly interpret the behaviour of the perovskite and to elucidate the anion exchange mechanisms.

In conclusion, we have developed a new versatile synthetic approach to grow a metal oxide shell around various NC cores. In particular $CsPbX_3@AlO_x$, $CeO_2@AlO_x$ and $Ag@AlO_x$ NCs were synthesized with tunable AlO_x shell thickness from 1 nm to 6 nm. The combination of different NC cores helped to elucidate the nucleation and growth of the alumina shell during the c-ALD process. In particular, FTIR highlights the need of oxygen,

whether on the surface or in the ligands, to initiate the c-ALD. Future engineering of the NC ligands with oxygen-rich groups would be interesting to further advance or generalize the developed c-ALD process. Finally, the $CsPbX_3@AlO_x$ NCs were exploited to get insights into the anion exchange reaction by in-situ XRD studies. Our results show that a transient structure is formed during the alloy process in both iodine and chlorine exchange reactions. The formation of this transient structure during the exchange is attributed to the existence of a certain mixed halide composition for which the alloy formation energy is minimized due to the strong ionic characters of halide perovskite materials. The anion exchange study performed in this work exemplifies the new opportunities offered by nm-thick metal oxide shell around active NC cores. The proposed systems could also act as materials platform to study solid-state ion diffusion across metal oxides, which is extremely interesting for perovskites solar cell, wherein an oxide layer acts both as electron or hole transporting layer to improve the charge transport and to reduce the instability issue due to diffusion of metal contact into the active perovskite layer.[50,51] In a more general prospective, the oxide shell could enable distance-dependent energy transfer studies between various donor and acceptor NCs (e.g. metal/semiconductor, semiconductor/semiconductor) as an alternative to using ligands of different lengths.[52,53]

ASSOCIATED CONTENT

Supporting Information. Information related to synthesis, additional EDX results and discussion, optical properties, FTIR data and discussion and additional XRD in-situ results. This material is available free of charge via the Internet at http://pubs.acs.org.

ACKNOWLEDGEMENT

A.L. and M. S. acknowledge a H2020-Marie Curie Individual Fellowship with grant numbers 701745 and 753124, respectively, for financial support. S.S. acknowledges the Swiss

National Science Foundation (AP Energy Grant, project number PYAPP2_166897/1). The XRD experiments were performed on the Swiss-Norwegian beamline BM01 at the European Synchrotron Radiation Facility (ESRF), Grenoble, France (proposal number: 01-02 1192). We are grateful to Dr. Diadkin Vadimat at ESRF for helpful discussions on the XRD data analysis. A. L. acknowledges Seyedebehnaz Varandili and Valerie A. Niemann for providing some of the nanocrystalline cores.

REFERENCES

( ) Yin, H.; Ma, Z.; Chi, M.; Dai, S. Heterostructured catalysts prepared by dispersing Au@Fe_2O_3 core–shell structures on supports and their performance in CO oxidation. *Catal. Today* **2011**, 160, 87 – 95.

(2) Mondal, K.; Sharma, A. Recent advances in the synthesis and application of photocatalytic metal–metal oxide core–shell nanoparticles for environmental remediation and their recycling process. *RSC Adv*. **2016**, 6, 83589 – 83612.

(3) Lu, J.; Fu, B.; Kung, M. C.; Xiao, G.; Elam, J. W.; Kung, H. H.; Stair, P. C. Coking and Sintering-Resistant Palladium Catalysts Achieved Through Atomic Layer Deposition. *Science* **2012**, 335, 1205 – 1208.

(4) O-Neill, B. J.; Jackson, D. H.; Crisci, K. A. J.; Farberow, C. A.; Shi, F.; Alba-Rubio, A. C.; Lu, J.; Dietrich, P. J.; Gu, X.; Marshall, C. L.; Stair, P. C.; Elam, J. W.; Miller, J. T.; Ribeiro, F. H.; Voyles, P. M.; Greeley, J.; Mavrikakis, M.; Scott, S. L.; Kuech, T. F.; Dumesic, J. A. Stabilization of Copper Catalysts for Liquid-Phase Reactions by Atomic Layer Deposition. *Angew. Chem. Int. Ed.* **2013**, 52, 13808 –13812.

(5) Chaudhuri, R. G.; Paria, S. Core/Shell Nanoparticles: Classes, Properties, Synthesis Mechanisms, Characterization, and Applications, *Chem. Rev.* **2012**, 112, 2373–2433.

(6) Guerrero-Martinez, A.; Perez-Juste, J.; Liz-Marzan, L. M. Recent progress on silica coating of nanoparticles and related nanomaterials. *Adv. Mater.* **2010**, 22, 1182−1195.

(7) Wang, H. C.; Lin, S. Y.; Tang, A. C.; Singh, B. P.; Tong, H. C.; Chen, C. Y.; Lee, Y. C.; Tsai, T. L.; Liu, R. S. Mesoporous Silica Particles Integrated with All-Inorganic CsPbBr3 Perovskite Quantum- Dot Nanocomposites (MP-PQDs) with High Stability and Wide Color Gamut Used for Backlight Display. *Angew. Chem., Int. Ed.* **2016**, 55, 7924−7929.

(8) Hu, H.; Wu, L.; Tan, Y.; Zhong, Q.; Chen, M.; Qiu, Y.; Yang, D.; Sun, B.; Zhang, Q.; Yin, Y. Interfacial Synthesis of Highly Stable $CsPbX_3$/Oxide Janus Nanoparticles. *J. Am. Chem. Soc.* **2018**, 140, 406−412.

(9) Rogach, A. L.; Nagesha, D.; Ostrander, J. W.; Giersig, M.; Kotov, N. A. "Raisin Bun"-Type Composite Spheres of Silica and Semiconductor Nanocrystals. *Chem. Mater.* **2000**, 12, 2676−2685.

(10) Loiudice, A.; Saris, S.; Oveisi, E.; Alexander, D. T. L.; Buonsanti, R. $CsPbBr_3$ QD/AlO_x Inorganic Nanocomposites with Exceptional Stability in Water, Light, and Heat. *Angew. Chem. Int. Ed.* **2017**,56,10696–10701.

(11) Liu, Y.; Gibbs, M.; Perkins, C. L.; Tolentino, J.; Zarghami, M. H.; Bustamante, J.; Law, M. Robust, Functional Nanocrystal Solids by Infilling with Atomic Layer Deposition. *Nano Lett.* **2011**, 11, 5349 –5355.

(12) Ephraim, J.; Lanigan, D.; Staller, C.; Milliron, D. J.; Thimsen, E. Transparent Conductive Oxide Nanocrystals Coated with Insulators by Atomic Layer Deposition. *Chem. Mater.* **2016**, 28, 5549 − 5553.

(13) Du, Y.-P.; Héroguel, F.; Luterbacher, J. S. Slowing the Kinetics of Alumina Sol-Gel Chemistry for Controlled Catalyst Overcoating and Improved Catalyst Stability and Selectivity. *Small* **2018**, 1801733.

(14) Ithurria, S.; Talapin, D. V. Colloidal Atomic Layer Deposition (c-ALD) using Self-Limiting Reactions at Nanocrystal Surface Coupled to Phase Transfer between Polar and Nonpolar Media. *J. Am. Chem. Soc.* **2012**, 134, 18585−18590.

(15) Nasilowski, M.; Nienhaus, L.; Bertram, S. N.; Bawendi, M. G. Colloidal atomic layer deposition growth of PbS/CdS core/shell quantum dots. *Chem. Commun.* **2017**, 53, 869 − 872.

(16) Oh, S. J.; Berry, N. E.; Choi, J.-H.; Gaulding, E. A.; Lin, H.; Paik, T.; Diroll, B. T.; Muramoto, S.; Murray, C. B., Kagan, C. R. Designing High-Performance PbS and PbSe Nanocrystal Electronic Devices through Stepwise, Post-Synthesis, Colloidal Atomic Layer Deposition. *Nano Lett.* **2014**, 14, 1559 − 1566.

(17) Sagar, L. K.; Walravens, W.; Zhao, Q.; Vantomme, A.; Geiregat, P.; Hens, Z. PbS/CdS Core/Shell Quantum Dots by Additive, Layer-by-Layer Shell Growth. *Chem. Mater.* **2016**, 28, 6953 − 6959.

(18) Routzahn, A. L.; Jain, P. K. Single-Nanocrystal Reaction Trajectories Reveal Sharp Cooperative Transitions. *Nano Lett.* **2014**, 14, 987 − 992.

(19) Luther, J. M.; Zheng, H.; Sadtler, B.; Alivisatos, A. P. Synthesis of PbS Nanorods and Other Ionic Nanocrystals of Complex Morphology by Sequential Cation Exchange Reactions. *J. Am. Chem. Soc.* **2009**, 131, 16851 − 16857.

(20) Andrew Nelson, Shreyas Honrao, Richard G. Hennig, Richard D. Robinson, Nanocrystal Symmetry Breaking and Accelerated Solid-State Diffusion in the Lead–Cadmium Sulfide Cation Exchange system. *Chem. Mater.* **2019**, 31, 3, 991 − 1005.

(21) van der Stam, W.; Berends, A. C.; Rabouw, F. T.; Willhammar, T.; Ke, X.; Meeldijk, J. D.; Bals, S.; de Mello Donega, C. Luminescent $CuInS_2$ Quantum Dots by Partial Cation Exchange in $Cu_{2-x}S$ Nanocrystals. *Chem. Mater.* **2015**, 27, 621 − 628.

(22) De Trizio, L.; Manna, L. Forging Colloidal Nanostructures via Cation Exchange Reactions. *Chem. Rev.* **2016**, 116, 10852 − 10887.

(23) Akkerman, Q. A.; D'Innocenzo, V.; Accornero, S.; Scarpellini, A.; Petrozza, A.; Prato, M.; Manna, L. Tuning the Optical Properties of Cesium Lead Halide Perovskite Nanocrystals by Anion Exchange Reactions. *J. Am. Chem. Soc.* **2015**, 137, 10276 − 10281.

(24) Nedelcu, G.; Protesescu, L.; Yakunin, S.; Bodnarchuk, M. I.; Grotevent, M. J.; Kovalenko, M. V. Fast Anion-Exchange in Highly Luminescent Nanocrystals of Cesium Lead Halide Perovskites ($CsPbX_3$, X = Cl, Br, I). *Nano Lett.* **2015**, 15, 5635 − 5640.

(25) Ramasamy, P.; Lim, D.; Kim, B.; Lee, S.; Lee, M.; Lee, J. All-inorganic cesium lead halide perovskite nanocrystals for photodetector applications. *Chem. Commun.* **2016**, 52, 2067 − 2070.

(26) Bekenstein, Y.; Koscher, B. A.; Eaton, S. W.; Yang, P.; Alivisatos, A. P. Highly Luminescent Colloidal Nanoplates of Perovskite Cesium Lead Halide and Their Oriented Assemblies. *J. Am. Chem. Soc.* **2015**, 137, 16008 − 16011.

(27) Creutz, S. E.; Crites, E. N.; De Siena, M. C.; Gamelin, D. R. Anion Exchange in Cesium Lead Halide Perovskite Nanocrystals and Thin Films using Trimethylsilyl Halide Reagents. *Chem. Mater.* **2018**, 30, 4887 − 4891.

(28) Creutz, S. E.; Crites, E. N.; De Siena, M. C.; Gamelin, D. R. Colloidal Nanocrystals of Lead-Free Double-Perovskite (Elpasolite) Semiconductors: Synthesis and Anion Exchange To Access New Materials. *Nano Lett.* **2018**, 18, 1118 − 1123.

(29) Zhang, J.; Yang, Y.; Deng, H.; Farooq, U.; Yang, X.; Khan, J.; Tang, J.; Song, H. High Quantum Yield Blue Emission from Lead-Free Inorganic Antimony Halide Perovskite Colloidal Quantum Dots. *ACS Nano* **2017**, 11, 9294 − 9302.

(30) Milstein, T.J.; Kluherz T.K.; Kroupa, D.M.; Erickson, C.S.; De Yoreo, J.J.; Gamelin, D.R. Anion Exchange and the Quantum-Cutting Energy Threshold in Ytterbium-Doped $CsPb(Cl_{1-x}Br_x)_3$ Perovskite Nanocrystals. *Nano Lett.* **2019**. in press.

(31) Yuan, Y.; Huang, J. Ion Migration in Organometal Trihalide Perovskite and Its Impact on Photovoltaic Efficiency and Stability. *Acc. Chem. Res.* **2016**, 49, 286 − 293.

(32) Hoke, E. T.; Slotcavage, D. J.; Dohner, E. R.; Bowring, A. R.; Karunadasa, H. I.; McGehee, M. D. Reversible photo-induced trap formation in mixed-halide hybrid perovskites for photovoltaics. *Chem. Sci.* **2015**, 6, 613 − 617.

(33) Snaith, H. J.; Abate, A.; Ball, J. M.; Eperon, G. E.; Leijtens, T.; Noel, N. K.; Stranks, S. D.; Wang, J. T.-E.; Wojciechowski, K.; Zhang, W. Anomalous Hysteresis in Perovskite Solar Cells. *J. Phys. Chem. Lett.* **2014**, 5, 1511 − 1515.

(34) Gratia, P.; Grancini, G.; Audinot, J.-N.; Jeanbourquin, X.; Mosconi, E.; Zimmermann, I.; Dowsett, D.; Lee, Y.; Grätzel, M.; De Angelis, F.; Sivula, K.; Wirtz, T.; Nazeeruddin, M. K. Intrinsic Halide Segregation at Nanometer Scale Determines the High Efficiency of Mixed Cation/Mixed Halide Perovskite Solar Cells. *J. Am. Chem. Soc.* **2016**, 138, 15821 – 15824.

(35) Tsai, H.; Asadpour, R.; Blancon, J.-C.; Stoumpos, C. C.; Durand, O.; Strzalka, J. W.; Chen, B.; Verduzco, R.; Ajayan, P. M.; Tretiak, S.; Even, J.; Ashraf Alam, Kanatzidis, M. M. G.; Nie, W.; Mohite, A. D. Light-induced lattice expansion leads to high-efficiency perovskite solar cells. *Science* **2018**, 360, 67 – 70.

(36) Koscher, B. A.; Bronstein, N. D.; Olshansky, J. H.; Bekenstein, Y.; Alivisatos, A. P. Surface- vs Diffusion-Limited Mechanisms of Anion Exchange in $CsPbBr_3$ Nanocrystal Cubes Revealed through Kinetic Studies. *J. Am. Chem. Soc.* **2016**, 138, 12065 − 12068.

(37) Pan, D.; Fu, Y.; Chen, J.; Czech, K. J.; Wright, J. C.; Jin, S. Visualization and Studies of Ion-Diffusion Kinetics in Cesium Lead Bromide Perovskite Nanowires. *Nano Lett.* **2018**, 18, 1807 − 1813.

(38) Lai, M.; Obliger, A.; Lu, D.; Kley, C. S.; Bischak, C. G.; Kong, Q.; Lei, T.; Dou, L.; Ginsberg, N. S.; Limmer, D. T.; Yang, P. Intrinsic anion diffusivity in lead halide perovskites is facilitated by a soft lattice. *PNAS* **2018**, 115, 11929 − 11934.

(39) Yin, W.-Y.; Yan, Y.; Wei, S.-H. Anomalous Alloy Properties in Mixed Halide Perovskites. *J. Phys. Chem. Lett.* **2014**, 5, 3625 − 3631.

(40) Protesescu, L.; Yakunin, S.; Bodnarchuk, M. I.; Krieg, F.; Caputo, R.; Hendon, C.; Yang, R. X.; Walsh, A.; Kovalenko, M. V. Nanocrystals of Cesium Lead Halide Perovskites ($CsPbX_3$, X = Cl, Br, and I): Novel Optoelectronic Materials Showing Bright Emission with Wide Color Gamut. *Nano Lett.* **2015**, 15, 3692 – 3696.

(41) Swarnkar, A.; Marshall, A. R.; Sanehira, E. M.; Chernomordik, B. D.; Moore, D. T.; Christians, J.A.; Chakrabarti, T.; Luther J. M. Quantum dot-induced phase stabilization of α-CsPbI3 perovskite for high-efficiency photovoltaics. *Science* **2016**, 354, 92 – 95.

(42) Lee, S. S.; Song, W.; Cho, M.; Puppala, H. L.; Nguyen, P.; Zhu, H.; Segatori, L.; Colvin, V. L. Antioxidant Properties of Cerium Oxide Nanocrystals as a Function of Nanocrystal Diameter and Surface Coating. *ACS Nano* **2013**, 7 (11), 9693 – 9703.

(43) Peng, S.; McMahon, J. M.; Schatz, G. C.; Gray, S. K.; Sun, Y. Reversing the size-dependence of surface plasmon resonances. *PNAS* **2010**, 107, 14530 – 14534.

(44) Rosen, E. L.; Buonsanti, R.; Llordes, A.; Sawvel, A. M.; Milliron, D. J.; Helms, B. A. Exceptionally Mild Reactive Stripping of Native Ligands from Nanocrystal Surfaces by Using Meerwein's Salt. *Angew. Chem., Int. Ed.* **2012**, 51, 684 – 691.

(45) Dyadkin, V.; Pattison, P.; Dmitriev, V.; Chernyshov, D. (IUCr) A new multipurpose diffractometer PILATUS@SNBL. *J. Synchrotron Radiat.* **2016**, 23, 825 – 829.

(46) Coelho, A. A. (IUCr.) Whole-profile structure solution from powder diffraction data using simulated annealing. *J. Appl. Crystallogr.* **2000**, 33 (3), 899 – 908.

(47) Kieffer, J.; Karkoulis, D. A versatile library for azimuthal regrouping, *J. Phys.: Conf. Ser.* **2013**, 425, 202012 – 2012017.

(48) Kuzma, A.; Weis, M.; Flickyngerova, S.; Jakabovic, J.; Satka, A.; Dobrocka, E.; Chlpik, J.; Cirak, J.; Donoval, M.; Telek, P.; Uherek, F.; Donoval, D. Influence of surface oxidation on plasmon resonance in monolayer of gold and silver nanoparticles. *J. Appl. Phys.* **2013**, 112, 103531 − 103536.

(49) Moore, W. M. Oxidation of silver films by atomic oxygen. *J. Phys. Chem.* **1988**, 92, 4421 − 4426.

(50) Li, J.; Dong, Q.; Li, N.; Wang, L. Direct Evidence of Ion Diffusion for the Silver-Electrode-Induced Thermal Degradation of Inverted Perovskite Solar Cells. *Adv. Energy Mater.* **2017**, 7 (14), 1602922 − 1602926.

(5) Kim, G. Y.; Senocrate, A.; Yang, T.; Gregori, G.; Grätzel, M.; Maier, J. Large Tunable Photoeffect on Ion Conduction in Halide Perovskites and Implications for Photodecomposition. *Nat. Mater.* **2018**, 17, 445 − 449.

(52) Akselrod, G. M.; Prins, F.; Poulikakos, L. V.; Lee, E. M. Y.; Weidman, M. C.; Mork, A. J.; Willard, A. P.; Bulović, V.; Tisdale, W. A. Subdiffusive Exciton Transport in Quantum Dot Solids. *Nano Lett.* **2014**, 14, 3556 − 3562.

(53) Yun, C. S.; Javier, A.; Jennings, T.; Fisher, M.; Hira, S.; Peterson, S.; Hopkins, B.; Reich, N. O.; Strouse, G. F. Nanometal Surface Energy Transfer in Optical Rulers, Breaking the FRET Barrier. *J. Am. Chem. Soc.* **2005**, 127, 3115 − 3119.

Table of Content